Coherently tunable metalens tweezers for optofluidic particle routing

SHENGQI YIN[1], FEI HE[1], WAKANA KUBO[2], QIAN WANG[3], JAMES FRAME[1],
NICOLAS G. GREEN[1] AND XU FANG[1,*]

[1]*School of Electronics and Computer Science, University of Southampton, SO17 1BJ, UK*
[2]*Division of Advanced Electrical and Electronics Engineering, Tokyo University of Agriculture and Technology, 2-24-16 Naka-cho, Koganei-shi, Tokyo 184-8588, Japan*
[3]*Institute of Materials Research and Engineering, Agency for Science, Technology and Research (A*STAR), 2 Fusionopolis Way, Innovis 08-03, Singapore 138634, Singapore*
**x.fang@soton.ac.uk*

Abstract: Nanophotonic particle manipulation exploits unique light shaping capabilities of nanophotonic devices to trap, guide, rotate and propel particles in microfluidic channels. Recent introduction of metalens into microfluidics research demonstrates the new capability of using nanophotonics devices for far-field optical manipulation. In this work we demonstrate, via numerical simulation, the first tunable metalens tweezers that function under dual-beam illumination. The phase profile of the metalens is modulated by controlling the relative strength and phase of the two coherent incident light beams. As a result, the metalens creates a thin sheet of focus inside a microchannel. Changes to the illumination condition allow the focus to be swept across the microchannel, thereby producing a controllable and reconfigurable path for particle transport. Particle routing in a Y-branch junction, for both nano- and microparticles, is evaluated as an example functionality for the tunable metalens tweezers. This work shows that tunable far-field particle manipulation can be achieved using near-field nano-engineering and coherent control, opening a new way for the integration of nanophotonics and microfluidics.

1. Introduction

Nanophotonic devices provide unprecedented levels of control over light waves via engineering light-matter interactions at the nanoscale. The integration of these devices with microfluidic systems enables advanced particle manipulation beyond the scope of conventional optical tweezers [1, 2]. Driven by this potential, a number of different nanophotonic devices have been explored, including waveguides [3], microrings [4], whispering gallery mode resonators [5, 6], photonic crystals [7], all-dielectric nanoantennas [8], and plasmonic resonators [9, 10]. All of these previous approaches achieve particle manipulation by exploiting electromagnetic near-field effects. Indeed, nanophotonics in the context of microfluidic applications is widely considered equivalent to "near field photonics" [11]. By comparison, recent exploration of metalens-based optical trapping [12-15] provides a new research direction: nanophotonic particle manipulation in the optical far field. A metalens is a metasurface (two dimensional metamaterial) that focuses light in the far field like a conventional glass lens, but achieves the required light bending with a subwavelength thickness [16]. In the context of optofluidics, metalens retains far-field particle manipulation capabilities of traditional optical tweezers (i.e. optical tweezers that rely on microscope objectives with a high numerical aperture), while it leverages the nanoscale light shaping capabilities provided by nanophotonic devices. This combination offers unique opportunities for advanced particle manipulation in lab-on-a-chip systems, as far-field optical control can now be engineered at the nanoscale.

This work represents the first study of tunable, metalens-based optical tweezers that function under dual-beam illumination. As opposed to the most common configuration of optical tweezers where a single incident light beam is used, dual-beam illumination employs two counter-propagating light beams. The combined optical force provided by the two incident beams has been used to trap macro-sized particles [17], stretch biological cells [18, 19], translate trapped particles along the beam axis [20-22], and even control their orientation in an optical trap [23]. Further exploration of the coherence between the two beams has enabled more advanced control such as particle translation with nanometer accuracy [24] and transferring optical angular momentum to trapped particles [25, 26]. In these previous works, the two incident light beams interact with the trapped particle directly. In contrast, this work employs two incident beams for a fundamentally different purpose: they are used to control the electromagnetic response of a metalens. The coherent interaction between the two incident beams and the metalens enables control over the phase profile of the metalens, which results in a steerable focus and consequent translation of trapped particles. This work is the first report that introduces coherent control of metasurfaces, a research area that has recently emerged from the development of tunable metamaterials [27], into the realm of microfluidics.

2. System design: metalens particle router

As a proof-of-principle demonstration, this work analyzes a tunable metalens-based particle router that can route fluid-borne particles in a Y-branch junction on demand, a functionality that resembles tunable optical tweezers (Fig. 1). The tunable metalens tweezers are an array of silicon nanopillars on top of a glass substrate (Figs. 1a and 1b). The unit cell (i.e. the smallest periodic unit of the metalens) is a row of 25 silicon nanopillars along the *x* axis (Fig. 1c), and the whole array is created by replicating this unit cell along the *y* direction at a periodicity of 900 nm. For all the nanopillars, the center-to-center distance between adjacent nanopillars is 900 nm, the height is 500 nm, and the cross section is elliptical. As shown in Fig. 1c and listed in Table 1, both the shape and dimensions of the cross section vary with the *x* position of the nanopillar, which is a key design feature of the metalens.

The metalens is covered by a layer of PDMS (polydimethylsiloxane) and positioned beneath a microfluidic channel (Fig. 1b). The microchannel has a width of 22.5 μm (in the *x* direction, matched to that of the metalens) and a base 130 μm above the metalens (in the *z* direction, defined from the middle height of the nanopillars). Water inside the microchannel moves slowly forward in the +*y* direction along the entrance section and predictably divides into the two branches, with the left and right half of the fluid moving towards Exit 1 and 2, respectively. Particles of interest, which are injected into the entrance section, pass above the metalens towards the branching point of the Y-branch junction. The metalens tweezers are designed to optically trap these particles in controlled positions in the *xz* cross-sectional plane, while leaving them free to move in the *y* direction. Particles trapped in the left and right half of the entrance section will be guided towards Exit 1 and 2, respectively, enabling the intended functionality of all-optical particle routing.

The particle trapping and routing (Fig. 1b) is achieved using coherent control. Coherent control, in the context of metamaterial and metasurface modulation, uses two coherent, counter-propagating light beams with controlled relative phase and strength as illumination [27]. A key aspect of coherent control/illumination is to create local electromagnetic field configurations that are unavailable for conventional plane waves [28]. The two most typical configurations are the E-antinode (electric field antinode) and the B-antinode (magnetic field antinode), where the local magnetic and electric field is always zero (i.e. a wave node), respectively. They are very different from conventional single-beam illumination, where both the electric and magnetic fields have finite magnitudes. These different field configurations can trigger different electromagnetic responses from a metasurface [29, 30]. In this case, the dual-beam illumination is used to create a tunable focus, with the E-antinode focus and the B-antinode focus guiding suspended particles towards different exits (Fig. 1d).

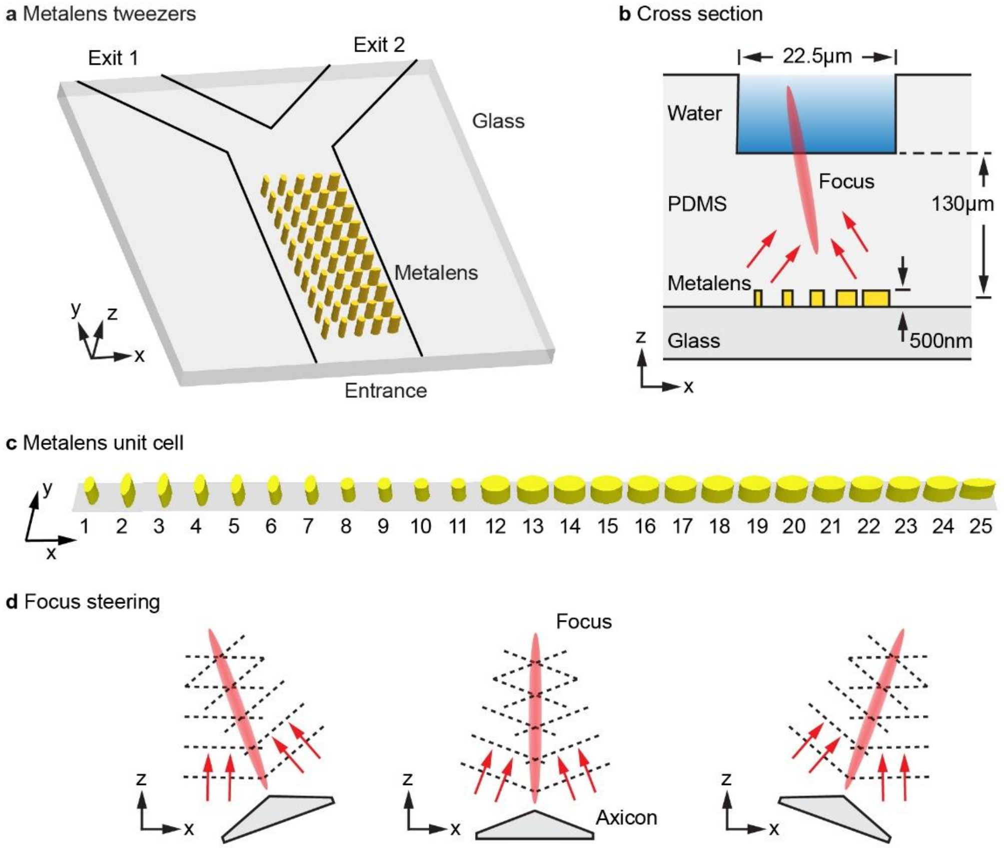

Fig. 1. Schematic diagram of tunable metalens tweezers and the application as an optofluidic particle router. (a) Schematic of the metalens, which is an array of Si nanopillars (in yellow color) on top of a glass substrate. The array has 25 nanopillars (only five are depicted here due to space constraint) in each row along the *x* axis, and the rows are identical along the *y* axis. The metalens lies beneath a microfluidic channel defined by a layer of PDMS (not depicted). The boundaries of the microchannel projected onto the glass substrate are indicated by the black lines. The microchannel has the shape of a Y-branch junction, consisting of one entrance and two exits. The intended functionality of the metalens tweezers is to define the *x* position of suspended particles in the entrance section, enabling routing towards either of the two exits. (b) Cross section of the device through the entrance channel. Under the illumination of two coherent, *x*-polarized, counter-propagating light beams at normal incidence (not depicted), constructive interference of light scattered by the nanopillars (red arrows) forms a focus inside the microchannel and the intermediate PDMS layer. The *xz* cross section of the focus approximates a Bessel beam. Several dimensions are annotated and the device is not drawn to scale. (c) Schematic of a single unit cell of the metalens, which consists of a row of 25 nanopillars. The figure is drawn to scale. (d) By using the technique of coherent control, the focus can be steered in the *xz* plane. The shape and the steering of the focus suggest that the tunable metalens behaves like a conventional cylindrical axicon lens that rotates in the *xz* plane.

The light focusing and particle trapping properties of the metalens were numerically evaluated by using a commercial finite element solver (Comsol Multiphysics). For all illumination conditions analyzed in this work, the incident light was linearly polarized along the *x* axis. The wavelength was 1550 nm, a telecommunications wavelength also frequently used in optofluidic experiments [31]. At this wavelength, the refractive indices of water, glass, PDMS and Si were set as 1.33, 1.50 (n_{Glass}), 1.40 (n_{PDMS}) and 3.48, respectively [32, 33]. The metalens was considered to be infinitely long in the *y* direction, approximating an entrance channel far away from the two exit branches. Following our previous work [30], all the illumination conditions were determined using the incident magnetic fields at the position of the metalens, where B_{Glass} and B_{PDMS} were for the incident light from the glass side and the PDMS side, respectively. The E-antinode condition corresponded to $B_{\mathrm{Glass}}/B_{\mathrm{PDMS}} = -n_{\mathrm{Glass}}/n_{\mathrm{PDMS}} = -1.50/1.40$ (the negative sign implied that the two fields were π out of phase), while the B-antinode condition corresponded to $B_{\mathrm{Glass}}/B_{\mathrm{PDMS}} = 1$ (the two fields were in phase). Two polystyrene spheres (refractive index = 1.56) [34], a nanosphere with a diameter of 100 nm and a microsphere with a diameter of 1 µm, were used to determine typical particle responses to the illumination. The optical force was first determined by integrating the Maxwell stress tensor at the surface of the particles using the simulated electromagnetic field. The trapping potential was then computed by integrating the force along a straight path as described in more detail in Section 4.

Table 1. Cross sectional dimensions of the 25 constituent nanopillars in nanometers. All the nanopillars have an elliptical cross section with the principal axes along *x* and *y*.

No.	*x* axis	*y* axis	No.	*x* axis	*y* axis	No.	*x* axis	*y* axis
1	120	250	10,11	170	170	17,18	380	235
2,3	130	350	12	350	253	19,20	380	230
4,5	130	310	13	380	245	21,22	380	220
6,7	140	270	14	380	242	23,24	380	210
8,9	160	190	15,16	380	240	25	400	130

3. Tailored phase response of constituent Si nanopillars

The metalens produces a focus due to the constructive interference of light scattered by the nanopillars, a process where the phase of the scattered light is of crucial importance. Figure 2 uses a specific nanopillar (nanopillar #1 in Fig. 1c and Table 1) as an example to demonstrate coherent control over the output phase. To simplify the phase extraction [35, 36], a uniform array (i.e. periodic along both the x and y axes) of same-sized nanopillars is simulated for this initial study. Both the PDMS layer and the glass substrate are treated as infinitely thick (i.e. the microfluidic channel is not considered at this stage, which is a good approximation due to the similarity between water and PDMS in their refractive indices). The spacing of the nanopillars is defined to be the same value of 900 nm as in the metalens (Fig. 2a). The array is illuminated by light at normal incidence, either from both the PDMS and the glass sides (Figs. 2b and 2d) or from only the PDMS side (Fig. 2c). The array scatters incident light both upwards (into the PDMS) and downwards (into the glass); only the former is analyzed here due to its relevance to particle manipulation. All the field maps (Figs. 2b-2d) show a plane wave propagating along the $+z$ direction, as only the zeroth-order diffraction is allowed for an effective wavelength (1107 nm in the PDMS) larger than the periodicity (900 nm). The output wave maintains the x polarization of the incident wave, as polarization rotation is forbidden by the planar symmetry.

As demonstrated previously in Ref. [30], two coherent, counter-propagating light waves illuminating an interface at normal incidence can form a standing wave, even if the media on the two sides of the interface have different refractive indices. If the interface is at the E-antinode (equivalently the B-node) of the standing wave (i.e. the illumination condition of Fig. 2b), the local electromagnetic field is purely electric. In contrast, if the interface is at the B-antinode (equivalently the E-node, the illumination condition of Fig. 2d), the local field is purely magnetic. A gradual transition from the E-antinode to the B-antinode can be achieved by maintaining one incident wave unchanged, while adjusting the phase and strength of the other incident wave. In this work, the incident wave from the PDMS side is chosen as the invariant wave (more detail in Section 4), and Fig. 2c corresponds to a specific case in the gradual transition where the other wave (i.e. the wave from the glass side) is switched off.

Figures 2b-2d show that the phase of the output light changes significantly with the illumination condition. The difference is 66.5° between the E-antinode and the single-beam conditions, and it reaches 174.5°, almost a total phase reverse of π, between the E-antinode and the B-antinode conditions. The phase shift clearly reveals that the optical properties of the Si nanopillar can be modulated through coherent control. This modulation originates from the fact that the nanopillar possesses multiple Mie resonances at this wavelength, where the electric dipole and magnetic dipole resonances are selectively dominant under the E-antinode and B-antinode conditions, respectively (see Fig. S1 for near-field analysis) [37]. Because different resonances impart different phase shift in light scattering, the nanopillar demonstrates a variable scattering phase controlled solely by means of the incident light.

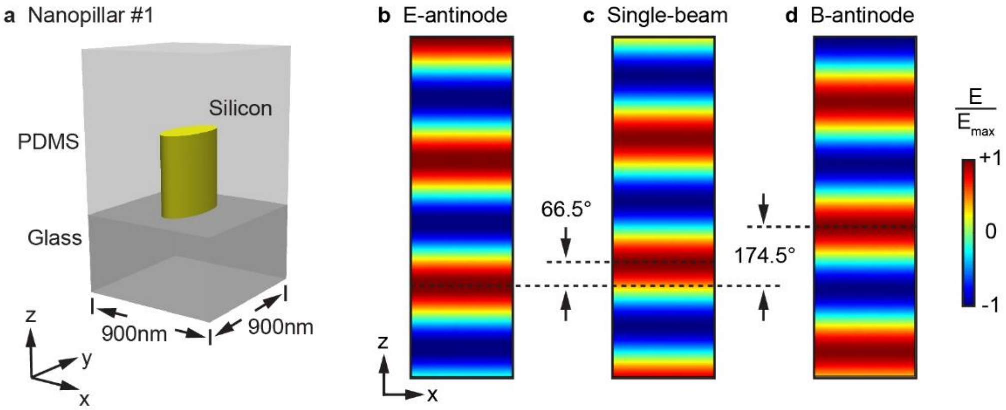

Fig. 2. Phase response in the output light from an example nanopillar. (a) Schematic of the nanopillar, which has an elliptical cross section with a width (along the *x* axis) of 120 nm and a length (along the *y* axis) of 250 nm. To determine the phase, a uniform array of the nanopillar, with periodicity = 900 nm in both the *x* and *y* directions, is simulated. The incident light propagates along the ±*z* directions. (b-d) Output electric field inside the PDMS, with the array (b) at the E-antinode of a standing wave formed by two incident light beams, (c) under the illumination of a single beam from the PDMS side, and (d) at the B-antinode of a standing wave. All three maps show the same area of 900 nm × 3 µm in the *xz* plane. The field is normalized against the maximum value in each individual figure.

A light-focusing metalens requires its constituent units (here the nanopillars) to exhibit a tailored phase profile across the whole metalens, and a tunable metalens further requires this phase profile to be modified in a designated fashion. In this work, both requirements are satisfied by adjusting the cross section of the nanopillars across the metalens. Following the same method discussed above for Fig. 2, nanopillars with 961 different cross sections are first simulated, with the dimensions along the *x* and *y* axis adjusted independently from each other from 100 to 400 nm at a step of 10 nm. Suitable nanopillars are then identified based on the strength (Fig. S2) and phase shift (discussed in detail below) in light scattering. As the result, the 25 nanopillars in a metalens unit cell adopt 15 different cross sections (Fig. 1c and Table 1). Reducing the dimension step from 10 nm to an even smaller value will increase the number of nanopillars available for selection, albeit also increasing the difficulty for future nanofabrication of the device.

Figures 3a-3c show the output electric field of the 25 nanopillars under three illumination conditions. In each figure, the 25 nanopillars are arranged in the order that they appear in the metalens unit cell (Figs. 2b-2d, which are for nanopillar #1, match with the first panel in Figs. 3a-3c). While these results are obtained from uniform arrays of same-sized nanopillars, they provide a useful initial step in designing the function of the metalens [37, 38]. All the 75 panels (25 pillars under 3 different illumination conditions) of Figs. 3a-3c show a plane wave propagating upwards away from the nanopillars. The vertical shift of the wave among these panels demonstrates that the phase of output light depends on both the geometry of the nanopillar and the illumination condition.

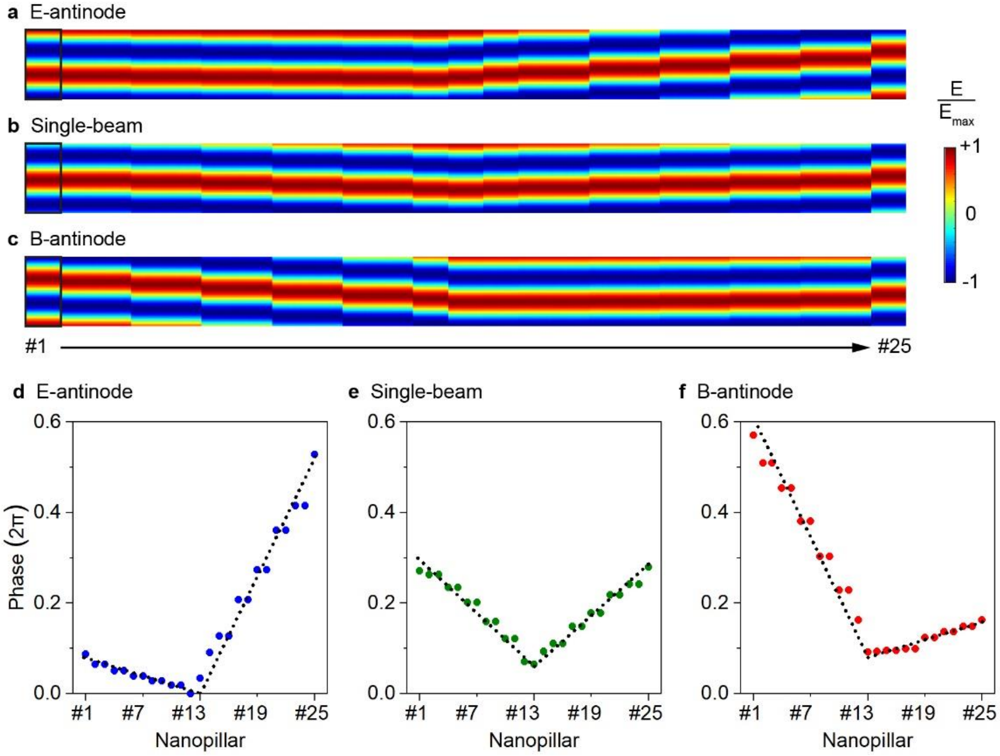

Fig. 3. Field distribution and phase shift of output light from uniform arrays of nanopillar #1 to #25. (a-c) Output electric field for three different illumination conditions. The panels are arranged as the nanopillars appear in the metalens unit cell. Each single panel (size highlighted for the first panel in each row with a black box) corresponds to the same area of 900 nm × 1.8 μm in the *xz* plane. The field is normalized against the maximum value in respective panel. (d-f) Values of phase extracted from corresponding field maps (dots), with the dashed lines as guide for the eye.

Figures 3d, 3e and 3f show the phase extracted from Figs. 3a, 3b and 3c, respectively. In each figure, the phase variation across the 25 pillars has roughly a V shape, with two straight lines intersecting at the center (i.e. at nanopillar #13). As the illumination condition changes from the E-antinode (Fig. 3d) to the B-antinode (Fig. 3f), the V shape rotates in the clockwise direction. This rotation results from the different illumination-induced phase shift among the nanopillars: the outer nanopillars (i.e. those closest to #1 and #25) have a larger shift than the inner nanopillars (i.e. those closest to #13), and the nanopillars on the left and on the right shift in opposite directions.

4. Coherently controlled light focusing and particle routing

As long as the near-field coupling between adjacent nanopillars is sufficiently weak and all the nanopillars have similar scattering strength (see Fig. S2 for details) [38], the light shaping performance of the metalens can be reasonably predicted based on the results in Fig. 3. This prediction is confirmed in Fig. 4, which shows the output of the metalens tweezers illustrated in Fig. 1. To better characterize the modulation in the output, in addition to the three illumination conditions discussed above (i.e. the E-antinode, the single-beam and the B-antinode conditions), Fig. 4 also includes two intermediate conditions. All the five conditions can be easily specified by the field ratio $B_{\mathrm{Glass}}/B_{\mathrm{PDMS}}$, which is -1.5/1.4, (1/2) × (-1.5/1.4), 0, 1/2 and 1 for Figs. 4a, 4b, 4c, 4d and 4e, respectively (note that 1.5/1.4 comes from $n_{\mathrm{Glass}}/n_{\mathrm{PDMS}}$ as discussed previously). All the conditions can be achieved by keeping the input beam from the PDMS side unchanged, while controlling the strength and phase of the beam from the glass side. Note that, the same as in Figs. 2 and 3, the field distribution shown here is purely the output field and contains no input field. Different from those two previous figures, the PDMS layer above the nanopillars is no longer treated as infinitely thick due to the inclusion of the microchannel in the simulation.

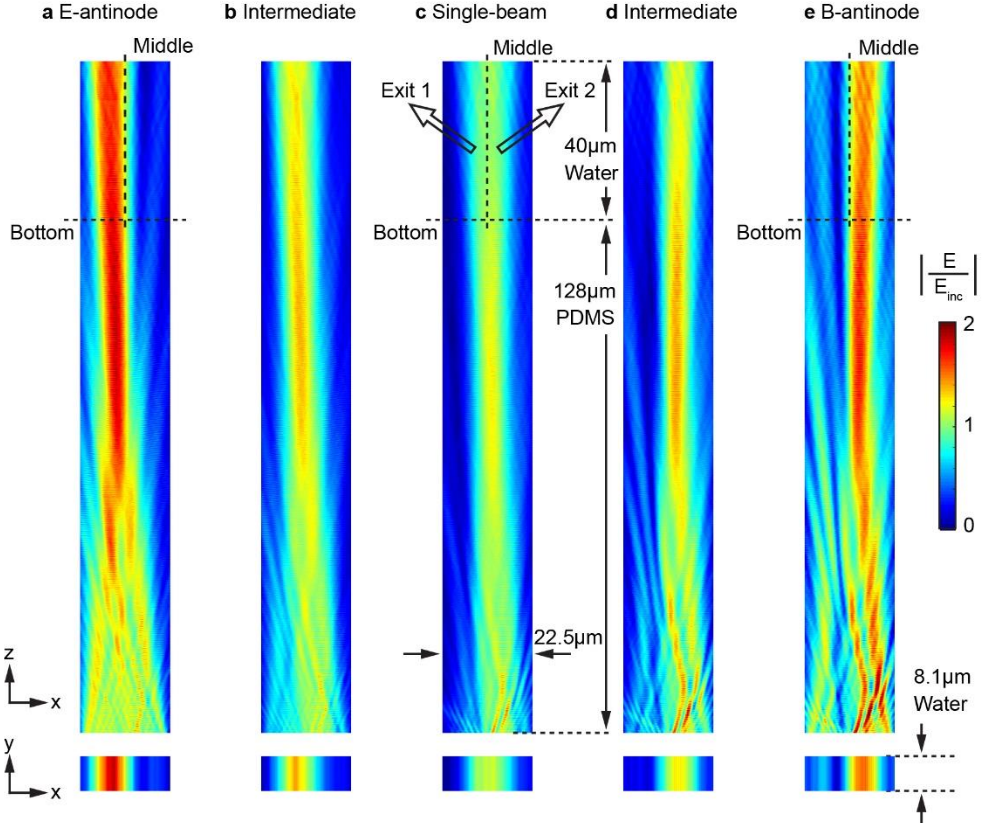

Fig. 4. Light focusing and steering of the metalens under (a-e) five different coherent illumination conditions, with the field ratio $B_{\mathrm{Glass}}/B_{\mathrm{PDMS}}$ equals (a) -1.5/1.4, (b) -1.5/2.8, (c) 0, (d) 0.5 and (e) 1. The maps in the top row show the electric field in the same area in the *xz* plane that bisects the middle of the nanopillars. These maps are 22.5 μm × 168 μm in size, with the bottom ~2 μm above the metalens. The base and the middle of the microchannel are highlighted in (a), (c) and (e). As water and PDMS are close in refractive index (1.33 versus 1.40), no reflection is discernible at the microchannel base. As opposed to the top row, the bottom row shows the field in the *xy* plane, with each map covering an area of 22.5 μm × 8.1 μm at 10 μm above the microchannel base. All the ten maps are normalized against the electric field of the incident light from the PDMS side, which is invariant with illumination condition. In consistence with the previous two figures, the maps do not contain any incident light or waterborne particle.

The top row of Fig. 4 shows the output field distribution in the *xz* plane (i.e. the cross section of the microchannel). Each map is 22.5 μm in width (the width of the metalens) and 168 μm in height (from 40 μm above the microchannel base to ~2 μm above the metalens). A long, narrow focus flanked by weak sidebands is observed. The focus is steered continuously, moving across the middle line of the microchannel from Fig. 4a to Fig. 4e. The angle between the central axis of the focus and the *z* axis is -1.37° and 1.36° in Figs. 4a and 4e, respectively, representing a steering angle of approximately 2.7°. The conversion efficiency, which is defined as the energy ratio of the main focus lobe and the total input, is 16.4% and 10.4% for the E-antinode focus and the B-antinode focus, respectively.

The bottom row of Fig. 4 shows the corresponding field distribution in the *xy* plane 10 μm above the microchannel base, for a range of 9 unit cells along the *y* axis. The distribution is independent of the *y* position for all the illumination conditions. This feature originates from the high uniformity of the nanopillars in the *y* direction: they are identical, and have a constant subwavelength spacing along each line in this direction. Such field distribution indicates that the focus creates a controllable and reconfigurable straight path for particle transport. It allows for the combined use of optical force and microfluidic flow, suitable for functionality such as routing where optical control is required only in directions orthogonal to fluid flow [10]. Target particles can even be actively collected to a designated transport path by sweeping the optical trap in the *xz* plane, as indicated by the continuous beam steering seen from Fig. 4a to Fig. 4e.

The elongated focus and its side bands in the *xz* plane (Fig. 4), together with the V-shaped phase profile (Fig. 3), resemble a Bessel-beam focus (see Fig. S3 for comparison). Bessel beams are produced traditionally using a glass axicon lens and more recently using a variety of metalenses (hence the terminology of axicon metalens and meta-axicon) [39-41]. They possess unique properties such as non-diffracting (i.e. capable of maintaining its transversal intensity profile in propagation) and self-healing (i.e. capable of recovering its original beam profile even if it is obstructed by a finite sized object), which are ideal for high-throughput particle manipulation [42-44]. The results in Figs. 3 and 4 demonstrate that the metalens functions like a steerable, cylindrical (referring to the invariant focus shape along the *y* direction) glass axicon lens that can be used as variable-position optical traps and tweezers.

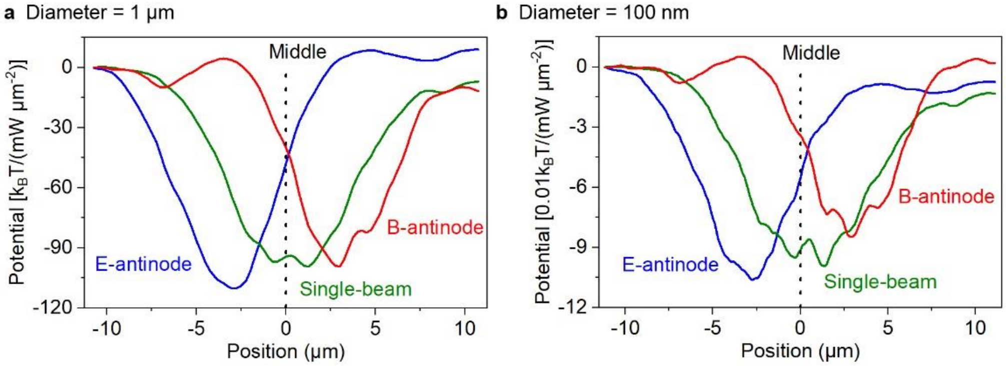

Fig. 5. Potential energy for trapping a single particle in the microchannel under three different illumination conditions. The particle diameter is (a) 1 μm and (b) 100 nm. In both cases, the center of the particle is kept at 10 μm above the microchannel base. The vertical dashed lines indicate the middle of the microchannel. The potential is normalized against the total incident power, and it is set as zero at the left end of all curves.

Based on the output field in Fig. 4, trapping potential is calculated for two example polystyrene particles, a microsphere with a diameter of 1 μm (Fig. 5a) and a nanosphere with a diameter of 100 nm (Fig. 5b), in the microchannel. In the calculation, both particles are swept from the left to the right boundary of the microchannel, at a height 10 μm above the channel base. The trapping potential along this straight line is then calculated with respect to the starting point. As seen in Fig. 5, for both particles, the bottom of the potential well appears in the left half of the channel (at $x \approx -2.5$ μm) for the E-antinode focus, while it moves to the right half (at $x \approx 2.5$ μm) for the B-antinode focus. This horizontal shift of the potential well clearly shows that coherent control enables particle routing. The depth of the potential well is roughly 100 and 0.1 $\mathrm{k_B \cdot T/(mW \cdot \mu m^{-2})}$ for the microsphere and nanosphere, respectively, where k_B is the Boltzmann constant and T is 297.15 K. It scales with the particle volume, as commonly observed in conventional optical traps (e.g. those created by focusing a single input beam using a microscope objective). As the trapping strength is sensitive to particle size, the routing functionality demonstrated here may be adopted for size-based sorting in the future, potentially by judicially balancing the optical trapping with microfluidic forces.

The trapping potential shown in Fig. 5 is derived from analyzing the interaction between the particles and the output field shown in Fig. 4, without considering any direct interaction between the particles and the incident light from the PDMS side. This is because that, being a plane wave, the incident light does not apply any force on the particles along the x axis, hence has no contribution to the x-axis trapping potential and the routing functionality. This analysis is based on the assumption that the incident wave reaches the metalens still as a plane wave, which is a good assumption for small particles (here diameters ≤ 1 μm) sparsely distributed far away (distance ≥ 130 μm) from the metalens.

5. Conclusion

To conclude, we have proposed and numerically evaluated a coherently controlled metalens that functions as tunable optical tweezers. Being an array of Si nano-pillars with a subwavelength thickness, the metalens focuses incident light into a thin sheet, which is similar to a cylindrical, axicon lens made of glass. The phase profile of the metalens can be coherently controlled, where the two counter-propagating incident light beams are adjusted in their relative phase and strength. This results in continuous steering of the focus across the microfluidic channel, enabling routing of both nano- and micro-sized particles in a Y-branch junction. Through modulating the response of the metalens, the coherent illumination enables controllable transverse (i.e. normal to the beam axis) particle steering, which has not been achieved in traditional dual-beam optical traps.

Metalens, as well as the broader concept of metasurface, enables novel light manipulation through nano-engineering, a capability that holds great promise for novel particle manipulation in next generation optofluidics and lab-on-a-chip systems. Although it no longer provides sub-wavelength focusing as seen in other nanophotonic platforms, metalens enables a very high level of flexibility in shaping the light field, as the far field distribution (here a steerable Bessel-beam focus) no longer has to trace the geometric shape (here an array of nano-pillars with fixed shape and dimensions) of the nanostructures. By demonstrating particle routing based on coherently tunable metalens tweezers, this work opens a new avenue for exploring the integration of nanophotonics and microfluidics.

Funding

Engineering and Physical Sciences Research Council (Doctoral Training Partnership studentship); Royal Society (IEC\R3\183071 and IES\R3\183086); Agency for Science, Technology and Research (1822430030).

Acknowledgements

The authors acknowledge the use of the IRIDIS High Performance Computing Facility, and associated support services at the University of Southampton, in the completion of this work.

Data availability

The data that support the findings will be available in the University of Southampton's ePrints research repository following an embargo from the date of publication.

Disclosures

The authors declare no conflicts of interest.

See Supplement 1 for supporting content.

References

1. D. Gao, W. Ding, M. Nieto-Vesperinas, X. Ding, M. Rahman, T. Zhang, C. Lim, and C. W. Qiu, "Optical manipulation from the microscale to the nanoscale: fundamentals, advances and prospects," Light Sci Appl 6, e17039 (2017).
2. J. E. Baker, R. P. Badman, and M. D. Wang, "Nanophotonic trapping: precise manipulation and measurement of biomolecular arrays," Nanomed Nanobiotechnol 10, e1477 (2018).
3. C. Pin, J. B. Jager, M. Tardif, E. Picard, E. Hadji, F. de Fornel, and B. Cluzel, "Optical tweezing using tunable optical lattices along a few-mode silicon waveguide," Lab Chip 18, 1750-1757 (2018).
4. S. Lin and K. B. Crozier, "Planar silicon microrings as wavelength-multiplexed optical traps for storing and sensing particles," Lab Chip 11, 4047-4051 (2011).
5. F. Vollmer and L. Yang, "Label-free detection with high-Q microcavities: a review of biosensing mechanisms for integrated devices," Nanophotonics 1, 267-291 (2012).
6. Y. Li, O. V. Svitelskiy, A. V. Maslov, D. Carnegie, E. Rafailov, and V. N. Astratov, "Giant resonant light forces in microspherical photonics," Light Sci Appl 2, e64 (2013).
7. S. H. Wu, N. Huang, E. Jaquay, and M. L. Povinelli, "Near-Field, On-Chip Optical Brownian Ratchets," Nano Lett 16, 5261-5266 (2016).
8. Z. Xu, W. Song, and K. B. Crozier, "Optical Trapping of Nanoparticles Using All-Silicon Nanoantennas," ACS Photonics 5, 4993-5001 (2018).
9. Y. Zhao, A. A. E. Saleh, and J. A. Dionne, "Enantioselective Optical Trapping of Chiral Nanoparticles with Plasmonic Tweezers," ACS Photonics 3, 304-309 (2016).
10. S. Yin, F. He, N. Green, and X. Fang, "Nanoparticle trapping and routing on plasmonic nanorails in a microfluidic channel," Opt Express 28, 1357-1368 (2020).
11. D. Erickson, X. Serey, Y. F. Chen, and S. Mandal, "Nanomanipulation using near field photonics," Lab Chip 11, 995-1009 (2011).
12. H. Markovich, Shishkin, II, N. Hendler, and P. Ginzburg, "Optical Manipulation along an Optical Axis with a Polarization Sensitive Meta-Lens," Nano Lett 18, 5024-5029 (2018).
13. G. Tkachenko, D. Stellinga, A. Ruskuc, M. Chen, K. Dholakia, and T. F. Krauss, "Optical trapping with planar silicon metalenses," Opt Lett 43, 3224-3227 (2018).
14. Y. Qin, Y. Li, D. Deng, Y. Liu, and M. Sun, "Ultracompact biosensor based on a metalens with a longitudinally structured vector beam," Appl Opt 58, 4438-4442 (2019).
15. Z. Shen, H. Liu, S. Zhang, Y. C. Shen, B. Zhang, and S. Luo, "Optical manipulation of Rayleigh particles by metalenses-a numerical study," Appl Opt 58, 5794-5799 (2019).
16. M. L. Tseng, H.-H. Hsiao, C. H. Chu, M. K. Chen, G. Sun, A.-Q. Liu, and D. P. Tsai, "Metalenses: Advances and Applications," Advanced Optical Materials 6, 1800554 (2018).
17. G. Thalhammer, R. Steiger, S. Bernet, and M. Ritsch-Marte, "Optical macro-tweezers: trapping of highly motile micro-organisms," Journal of Optics 13, 044024 (2011).
18. J. G. e. al, "Stretching biological cells with light," J Phys Condens Mat 14, 4843-4856 (2002).
19. F. B. Nicola Bellini, I. Cristiani, J. Guck, R. Osellame, and G. Whyte, "Validation and perspectives of a femtosecond laser fabricated monolithic optical stretcher," Biomedical Opt Express 3, 2658-2668 (2012).
20. K. Wang, E. Schonbrun, P. Steinvurzel, and K. B. Crozier, "Scannable plasmonic trapping using a gold stripe," Nano Lett 10, 3506-3511 (2010).
21. O. G. Helleso, P. Lovhaugen, A. Z. Subramanian, J. S. Wilkinson, and B. S. Ahluwalia, "Surface transport and stable trapping of particles and cells by an optical waveguide loop," Lab Chip 12, 3436-3440 (2012).
22. R. An, G. Wang, W. Ji, W. Jiao, M. Jiang, Y. Chang, X. Xu, N. Zou, and X. Zhang, "Controllable trapping and releasing of nanoparticles by a standing wave on optical waveguides," Opt Lett 43, 3901-3904 (2018).
23. M. Kreysing, D. Ott, M. J. Schmidberger, O. Otto, M. Schurmann, E. Martin-Badosa, G. Whyte, and J. Guck, "Dynamic operation of optical fibres beyond the single-mode regime facilitates the orientation of biological cells," Nat Commun 5, 5481 (2014).
24. M. Soltani, J. Lin, R. A. Forties, J. T. Inman, S. N. Saraf, R. M. Fulbright, M. Lipson, and M. D. Wang, "Nanophotonic trapping for precise manipulation of biomolecular arrays," Nat Nanotechnol 9, 448-452 (2014).
25. O. Brzobohaty, A. V. Arzola, M. Siler, L. Chvatal, P. Jakl, S. Simpson, and P. Zemanek, "Complex rotational dynamics of multiple spheroidal particles in a circularly polarized, dual beam trap," Opt Express 23, 7273-7287 (2015).
26. M. G. Donato, O. Brzobohaty, S. H. Simpson, A. Irrera, A. A. Leonardi, M. J. Lo Faro, V. Svak, O. M. Marago, and P. Zemanek, "Optical Trapping, Optical Binding, and Rotational Dynamics of Silicon Nanowires in Counter-Propagating Beams," Nano Lett 19, 342-352 (2019).
27. E. Plum, K. F. MacDonald, X. Fang, D. Faccio, and N. I. Zheludev, "Controlling the Optical Response of 2D Matter in Standing Waves," ACS Photonics 4, 3000-3011 (2017).
28. X. Fang, K. F. MacDonald, E. Plum, and N. I. Zheludev, "Coherent control of light-matter interactions in polarization standing waves," Sci Rep 6, 31141 (2016).
29. X. Fang, M. L. Tseng, D. P. Tsai, and N. I. Zheludev, "Coherent Excitation-Selective Spectroscopy of Multipole Resonances," Physical Review Applied 5, 014010 (2016).
30. F. He, K. F. MacDonald, and X. Fang, "Coherent illumination spectroscopy of nanostructures and thin films on thick substrates," Opt Express 26, 12415-12424 (2018).
31. P. Minzioni, R. Osellame, C. Sada, S. Zhao, F. G. Omenetto, K. B. Gylfason, T. Haraldsson, Y. Zhang, A. Ozcan, A. Wax, F. Mugele, H. Schmidt, G. Testa, R. Bernini, J. Guck, C. Liberale, K. Berg-Sørensen, J. Chen, M.

Pollnau, S. Xiong, A.-Q. Liu, C.-C. Shiue, S.-K. Fan, D. Erickson, and D. Sinton, "Roadmap for optofluidics," Journal of Optics 19, 093003 (2017).

32. V. Prajzler, W. Jung, K. Oh, J. Cajzl, and P. Nekvindova, "Optical properties of deoxyribonucleic acid thin layers deposited on an elastomer substrate," Optical Materials Express 10, 421-433 (2020).
33. E. D. Palik, *Handbook of optical constants of solids* (Academic Press, 1985).
34. X. Zhang, J. Qiu, X. Li, J. Zhao, and L. Liu, "Complex refractive indices measurements of polymers in visible and near-infrared bands," Appl Opt 59, 2337-2344 (2020).
35. S. Sun, K. Y. Yang, C. M. Wang, T. K. Juan, W. T. Chen, C. Y. Liao, Q. He, S. Xiao, W. T. Kung, G. Y. Guo, L. Zhou, and D. P. Tsai, "High-efficiency broadband anomalous reflection by gradient meta-surfaces," Nano Lett 12, 6223-6229 (2012).
36. Y. F. Yu, A. Y. Zhu, R. Paniagua-Domínguez, Y. H. Fu, B. Luk'yanchuk, and A. I. Kuznetsov, "High-transmission dielectric metasurface with 2π phase control at visible wavelengths," Laser & Photonics Reviews 9, 412-418 (2015).
37. F. He, K. F. MacDonald, and X. Fang, "Continuous beam steering by coherent light-by-light control of dielectric metasurface phase gradient," Optics Express 28, 30107-30116 (2020).
38. S. M. Kamali, E. Arbabi, A. Arbabi, and A. Faraon, "A review of dielectric optical metasurfaces for wavefront control," Nanophotonics 7, 1041-1068 (2018).
39. F. Aieta, P. Genevet, M. A. Kats, N. Yu, R. Blanchard, Z. Gaburro, and F. Capasso, "Aberration-free ultrathin flat lenses and axicons at telecom wavelengths based on plasmonic metasurfaces," Nano Lett 12, 4932-4936 (2012).
40. D. Lin, P. Fan, E. Hasman, and M. L. Brongersma, "Dielectric gradient metasurface optical elements," Science 345, 298-302 (2014).
41. W. T. Chen, M. Khorasaninejad, A. Y. Zhu, J. Oh, R. C. Devlin, A. Zaidi, and F. Capasso, "Generation of wavelength-independent subwavelength Bessel beams using metasurfaces," Light Sci Appl 6, e16259 (2017).
42. M. Mazilu, D. J. Stevenson, F. Gunn-Moore, and K. Dholakia, "Light beats the spread: “non-diffracting” beams," Laser & Photonics Reviews 4, 529-547 (2010).
43. Y. A. Ayala, A. V. Arzola, and K. Volke-Sepúlveda, "Comparative study of optical levitation traps: focused Bessel beam versus Gaussian beams," Journal of the Optical Society of America B 33, 1060-1067 (2016).
44. Y. Liang, S. Yan, B. Yao, and M. Lei, "Direct observation and characterization of optical guiding of microparticles by tightly focused non-diffracting beams," Opt Express 27, 37975-37985 (2019).